

# Stability and Migration of Slab-Derived Carbonate-rich Melts above the Transition Zone

Yizhuo Sun<sup>a,b,c</sup>, Saswata Hier-Majumder<sup>b</sup>, Yigang Xu<sup>a</sup>, Michael Walter<sup>d</sup>

<sup>a</sup>*State Key Laboratory of Isotope Geochemistry, Guangzhou Institute of Geochemistry, Chinese Academy of Sciences, Guangzhou 510640, China*

<sup>b</sup>*Department of Earth Sciences, Royal Holloway University of London, Egham, Surrey, TW20 0EX, UK*

<sup>c</sup>*University of Chinese Academy of Sciences, Beijing 100049, China*

<sup>d</sup>*Geophysical Laboratory, Carnegie Institution of Washington, Washington, D.C. 20015, USA*

---

## Abstract

We present a theoretical model of the stability and migration of carbonate-rich melts to test whether they can explain seismic low-velocity layers (LVLs) observed above stalled slabs in several convergent tectonic settings. The LVLs, located atop the mantle transition zone, contain small ( $\sim 1\text{vol}\%$ ) amounts of partial melt, possibly derived from melting of subducted carbonate-bearing oceanic crust. Petrological and geochemical evidence from inclusions in superdeep diamonds supports the existence of slab-derived carbonate melt, which may potentially explain the origin of the observed melt in the LVL. However, the presumptive reducing nature of the ambient mantle can be an impediment to the stability of carbonated melt. To reconcile this apparent contradiction, we test the stability and migration rates of carbonate-rich melts atop a stalled slab as a function of melt percolation, redox freezing, amount of carbon supplied by subduction, and the metallic Fe concentration

---

*Email address:* `saswata.hier-majumder@rhul.ac.uk` (Saswata Hier-Majumder )

in the mantle. Our results demonstrate that carbonate-rich melts in the LVL can potentially survive redox freezing over long geological time scales. We also show that the amount of subducted carbon exerts a stronger influence on the stability of carbonate melt than does the mantle redox condition. Concentration dependent melt density leads to rapid melt propagation through channels while a constant melt density causes melt to migrate as a planar front. Our calculations suggest that the LVLs can sequester significant fractions of carbon transported to the mantle by subduction.

*Keywords:* Transition Zone; Low-velocity Layer; Carbonate-rich Melts; Volatile Cycle; Reactive Porous Flow

---

## 1. Introduction

The Earth's deep interior can host a significant quantity of carbon, with estimates for the amount of carbon sequestered in the deep Earth reaching up to an order of magnitude larger than the carbon content of the atmosphere (Hirschmann and Dasgupta, 2009). Currently, the Earth's exosphere contains nearly twice as much H by mass as C, while the H:C ratio in chondrites is only 0.55 (Hirschmann and Dasgupta, 2009). This discrepancy indicates that the Earth's deep interior could be a considerable repository of C, estimated to be  $\sim 10^{20}$  kg (Dasgupta and Hirschmann, 2010). Direct evidence for the presence of C in the Earth's convecting mantle comes from sublithospheric or 'superdeep' diamonds. The mineralogical and chemical signature of mineral inclusions, together with symmetric internal structure and low density of crystal defects of the diamond hosts, indicate that they crystallized from carbon-rich melts in the mantle (Bulanova et al., 2010; Harte, 2010; Walter

et al., 2008). The abundance of superdeep diamonds exhibiting isotopically light carbon relative to the mantle value, together with mineral inclusions exhibiting isotopically heavy oxygen, also suggests that the carbonate-rich melt from which they crystallized was derived from subducted oceanic crustal materials (Bulanova et al., 2010; Burnham et al., 2015; Ickert et al., 2015; Thomson et al., 2014). The geochemical and petrological evidence for deep carbonated melt is complemented by seismological observations of anomalous regions above the mantle transition zone (MTZ) that have properties indicating the likely presence of partial melt. We postulate that these melt-containing regions can act as potential sites for transfer or accumulation in the mantle of carbon from subducting slabs.

A number of seismic studies identified, mostly on a regional scale, the presence of a low-velocity layer (LVL) located at a depth of approximately 350 km in a number of different tectonic settings (Agius et al., 2017; Tauzin et al., 2010, 2017; Wei and Shearer, 2017). The LVLs are marked by a 2–3 % reduction in shear wave speed and a sharp interface with the overlying mantle, suggesting the presence of partial melt (Hier-Majumder and Courtier, 2011; Hier-Majumder et al., 2014; Hier-Majumder and Tauzin, 2017). A number of seismic studies of the LVLs also report the temperature sensitive thickness of the mantle transition zone at the LVL sites (Agius et al., 2017; Tauzin et al., 2017). Combined analysis of the seismic wavespeed reduction and temperature derived from the MTZ thickness suggest that the LVL contains small amounts (0.5 – 1 vol%) of partial melt (Hier-Majumder and Courtier, 2011; Hier-Majumder et al., 2014; Hier-Majumder and Tauzin, 2017).

A comparison between the occurrence of LVLs and the location of earth-

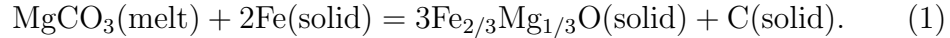
40 quakes along subducting plates demonstrates that a large number of LVLs  
 41 are associated with subduction zones or continental collision zones. The map  
 42 in Figure 1(a) outlines a cluster of LVLs along both margins of the Pacific.  
 43 As the subducting slab penetrates the MTZ, geodynamic modelling suggests  
 44 that slab stagnation and deflection arises from variations in density, viscosity,  
 45 and the Clapeyron slopes of phase-transition at the base of the mantle transi-  
 46 tion zone (Christensen, 2001; Christensen and Yuen, 1984). Slab stagnation  
 47 in the transition zone is often accompanied by trench retreat and high trench  
 48 migration rates promote flattening of the slab (Christensen, 1996; Čížková  
 49 et al., 2002; Griffiths et al., 1995) as shown in Figure 1(b). Seismic obser-  
 50 vations of the mantle beneath the western USA and East Asia further show  
 51 such stalling of the subducting plate at the MTZ (Tauzin et al., 2017, 2013).

52 The temperature of the LVL from seismic studies, however, is too cold to  
 53 melt mantle peridotite without the presence of volatile components such as  
 54  $\text{CO}_2$  or  $\text{H}_2\text{O}$ . Petrological experiments on carbonate-bearing basalts indicate  
 55 that the melting temperature of such rocks are sharply reduced at transition  
 56 zone depths (Thomson et al., 2016). Figure 1(c) plots the solidi of carbonated  
 57 basalt, hydrated and dry peridotites. The figure also includes hot and cold  
 58 subduction slab-top geotherms (Turcotte and Schubert, 2001, Ch. 4) as well  
 59 as the depth and range of temperature calculated from the mantle transition  
 60 zone thickness in the western US (Hier-Majumder and Tauzin, 2017). The  
 61 coincidence of slab-top geotherms, seismically inferred P-T conditions, and  
 62 the solidus of carbonated basalts from Thomson et al. (2016) demonstrates  
 63 that slab melting induced by  $\text{CO}_2$  can potentially provide an explanation for  
 64 the observed melting within the LVLs associated with subduction zones (Li



et al., 2017; Thomson et al., 2016; Xu et al., 2018). In addition, the location of the LVL beneath Eastern China (Tauzin et al., 2017) partially coincides with locations of basalts with low  $\delta^{26}\text{Mg}$  values, attributed to reaction between slab-derived carbonated melts and mantle peridotites (Li et al., 2017).

One issue with the hypothesis of carbonated melts in the LVLs arises from the fact that such melts might be chemically unstable due to the predicted low oxygen fugacity of the mantle at these depths. Experiments by Rohrbach and Schmidt (2011) on the mantle redox state of peridotite at such depths suggest that carbonated melt in the deep mantle ( $> 250$  km) can be reduced to diamond due to the low oxygen fugacity and the saturation of metallic iron, following a reaction similar to (Dorfman et al., 2018)



Reactions involving slab derived carbonate-rich melt and the surrounding mantle have been postulated on the basis of chemical evidence from inclusions in superdeep diamonds (Bulanova et al., 2010; Thomson et al., 2014, 2016; Walter et al., 2008). Whether the  $f_{\text{O}_2}$  of the mantle is sufficiently reducing or whether enough Fe is present to completely consume slab derived, carbonate-rich melts, however, remains an open question. The magnitude of melt-bound carbon fluxes into the mantle also remains a poorly constrained quantity.

This article is motivated by these complementary constraints on the deep carbon cycle arising from seismic, petrological, and geochemical observations. To better understand the fate of slab-derived, carbonate-rich melts subjected to redox freezing as predicted by experimental petrology, and to test the plausibility of such melts in producing the LVLs, here we investigate the stability of a reactive, slab-derived, carbonate-rich melt in the mantle. In

our model, we treat the LVL as a two-dimensional region containing 1 vol% porosity filled by melts and embedded in a mantle containing free Fe that reacts with the carbonate in the melt supplied by the subducting slab (Figure 1(d)). Using numerical simulations and analytical solutions, we calculate the CO<sub>2</sub> flux from the slab to the mantle and the mode of melt transport from the slab to the LVL. In the following sections, we outline the formulation of our model, present the results, and discuss the implications for the global carbon cycle.

## 2. Formulation

We formulate the problem of the stability of carbonate-rich partial melts in a reducing mantle in the context of the transport of a dissolved chemical component (carbonate) by advective-diffusive-reactive transport (Ghesmat et al., 2011; Unwin et al., 2016) in the presence of a source. The physical processes and parameters that control the stability of the carbonate melt in the mantle are: the relative rate of reaction and melt percolation, rate of carbonate supply from slab, the free Fe content in the LVL, and the relative rate of melt percolation and diffusion of carbonate. The schematic diagrams in Figures 1(b) and (d) illustrates our model in the context of subducting lithosphere and the global carbon cycle. The 2D problem is defined within a rectangular domain with a carbonate-rich melt source located at the bottom, mimicking the supply from a stalled subducting slab. The porosity or the melt fraction of this domain is set at 1 vol%, since the LVL contains 1 vol% partial melt distributed uniformly, according to the seismic observations (Hier-Majumder and Courtier, 2011; Hier-Majumder and Tauzin, 2017). We

113 also prescribe a uniform initial distribution of Fe in the LVL mantle. We  
 114 numerically model the evolution of carbonate concentration in the LVL us-  
 115 ing a finite element formulation and predict the growth rate of perturbations  
 116 analytically using a marginal stability analysis of linearized equations.

### 117 *2.1. Governing equations*

118 In our advection-diffusion-reaction model, porous flow of the carbonate-  
 119 rich fluid is controlled by the gradient of pore fluid pressure and the density  
 120 contrast between the melt and the surrounding mantle. For a constant melt  
 121 volume fraction,  $\phi$ , the velocity of the melt,  $\mathbf{u}$ , is governed by Darcy flow. We  
 122 make the Boussinesq approximation in our simulations, such that the density  
 123 changes only influence the momentum (Darcy flow) without influencing the  
 124 mass of the melt. These two conditions can then be described in a domain  
 125  $\Omega \subset \mathbb{R}^d, 1 \leq d \leq 3$ , as

$$\phi \mathbf{u} = -\frac{\kappa}{\mu} (\nabla p' + \rho g \hat{\mathbf{z}}), \quad (2)$$

126 and

$$\nabla \cdot \mathbf{u} = 0, \quad (3)$$

127 where  $\kappa$  is the permeability of the matrix,  $\mu$  is the dynamic viscosity of  
 128 the melt,  $p'$  is the pore-fluid pressure,  $\rho$  is the density of the melt,  $g$  is the  
 129 gravitational acceleration, and  $\hat{\mathbf{z}}$  is a unit vector in the vertically upward  
 130 direction.

131 The concentration of carbonate in the melt,  $c$ , can affect the density of  
 132 the fluid (Duncan and Agee, 2011). We assume a linear variation of the form,

$$\rho = \rho_0 + \gamma_0 c, \quad (4)$$

133 where  $\rho_0$  is the density of the carbonate-free melt, and the constant  $\gamma_0 < 0$ ,  
 134 indicating the density of the melt decreases with an increase in the concen-  
 135 tration of dissolved carbonate. We also define  $\Delta\rho = \rho_s - \rho$ , where  $\rho_s$  is  
 136 the density of the solid. In order to illustrate the effect of carbonate con-  
 137 centration on the melt directly, we also define the total pressure,  $p$ , as the  
 138 sum of fluid pressure and the lithostatic pressure (e.g. Hier-Majumder, 2018;  
 139 Rhebergen et al., 2014), given by,

$$p = p' + \rho_s g z. \quad (5)$$

140 Combining the definition of  $\Delta\rho$  and reduced pressure from equation (5), we  
 141 can write the modified Darcy equation as,

$$\phi \mathbf{u} = -\frac{\kappa}{\mu} [\nabla p - \Delta\rho_0 (1 - \gamma^* c) g \hat{\mathbf{z}}], \quad (6)$$

142 where  $\Delta\rho_0 = \rho_s - \rho_0$ , and  $\gamma^* = \gamma_0/\Delta\rho_0$ . In problems of density-driven fluid  
 143 migration, this substitution is often used to highlight the role played by the  
 144 density difference between the solid and the pore fluid (Aharonov et al., 1995;  
 145 Hier-Majumder et al., 2006; Rhebergen et al., 2014; Spiegelman et al., 2001;  
 146 Takei and Hier-Majumder, 2009; Unwin et al., 2016). In the presence of  
 147 compaction of the matrix, which we do not consider in this work, a more  
 148 generalized form of this equation is given by an action-reaction equation.  
 149 Interested readers can see Bercovici et al. (2001) for a detailed derivation of  
 150 the coupled governing equations of two phases.

151 The next set of governing equations arise from the mass conservation of  
 152 chemical components (Aharonov et al., 1995; Bercovici et al., 2001; Ghesmat  
 153 et al., 2011; Spiegelman et al., 2001; Steefel and Lasaga, 1994; Takei and  
 154 Hier-Majumder, 2009). The chemical reaction in equation (1) affects the

155 concentration of the components. We assign the variables  $c$  and  $c_F$  for con-  
 156 centration of  $\text{MgCO}_3$  in the melt and Fe in the solid, respectively. Assuming  
 157 the rate of the chemical reaction is driven by the faster, fluid assisted forward  
 158 reaction, the solidification rates for the dissolved carbonate component in the  
 159 melt and the free Fe in the mantle are respectively defined as  $\Gamma_c = \Gamma_0 c c_F^2$  and  
 160  $\Gamma_F = \alpha \Gamma_0 c c_F^2$ , where  $\Gamma_0$  is a constant and  $\alpha = M_{\text{MgCO}_3}/(2M_{\text{Fe}}) \approx 0.75$  is the  
 161 ratio of molecular weight multiplied by the coefficients of the reactants in the  
 162 reaction in equation (1). The concentration of carbonate in the melt within  
 163 the LVL is also influenced by input from the subducting slab. We prescribe  
 164 a function  $f_c$  as a source term for the advection diffusion reaction equation.  
 165 The initial concentration of Fe in the mantle is fixed, but changes as Fe is  
 166 consumed by reaction with the carbonate in the melt. Taking these into  
 167 account, the mass conservation equations for these two chemical components  
 168 are described by,

$$\phi \frac{\partial c}{\partial t} + \phi \mathbf{u} \cdot \nabla c = \phi D \nabla^2 c - \Gamma_c + f_c, \quad (7)$$

169 and

$$(1 - \phi) \frac{\partial c_F}{\partial t} = -\Gamma_F, \quad (8)$$

170 where  $t$  is time and  $D$  is the diffusivity of carbon in the melt. As equation  
 171 (7) illustrates, the rate of change in concentration of carbonate in the LVL  
 172 depends on transport by porous flow (second term on the left), diffusion,  
 173 chemical reaction, and input from subduction. Consumption of Fe, given by  
 174 equation (8), is only controlled by reaction with carbonate in the melt.

175 The source term,  $f_c$ , is spatially variable. As the carbonate input from  
 176 the slab is confined near the bottom of the LVL, we prescribe the lateral

177 variation of  $f_c$  as a sum of positive sine waves,

$$f_c = f_0(1 - \tanh(100z)) \left[ \frac{1}{10} \sum_{j=1}^{20} |\sin(j\pi x)| \right], \quad (9)$$

178 the tanh function constrains the source term near the bottom of the domain.  
 179 The schematic diagram in Figure 1(d) shows a colormap of the source term  
 180 in the background.

181 To solve the governing PDEs, we impose a set of Dirichlet, Neumann, and  
 182 periodic boundary conditions on the primary unknowns,  $\mathbf{u}$  and  $c$ . We set the  
 183 vertical walls of the domain,  $\partial\Omega_v$ , as periodic boundaries in both  $\mathbf{u}$  and  $c$ ,  
 184 impose a Dirichlet condition on  $\mathbf{u}$  at the slab-LVL interface at the bottom  
 185 boundary,  $\partial\Omega_b$ , and free boundary at the top,  $\partial\Omega_t$ . We impose a zero diffusive  
 186 flux Neumann condition on  $c$  at the Neumann boundary  $\partial\Omega_N = \partial\Omega_b \cup \partial\Omega_t$ .  
 187 The complete set of boundary conditions are given by,

$$\mathbf{u} = w_0 \hat{\mathbf{z}} \text{ on } \partial\Omega_b, \quad (10)$$

$$\mathbf{u}, c = \text{periodic on } \partial\Omega_v, \quad (11)$$

$$\nabla c \cdot \hat{\mathbf{n}} = 0 \text{ on } \partial\Omega_N \quad (12)$$

188 where  $w_0$  is the magnitude of prescribed melt velocity. Using the conserva-  
 189 tive estimate of boundary melt velocity of 100  $\mu\text{m}/\text{yr}$  (Hier-Majumder and  
 190 Tauzin, 2017) combined with the dimensional value of  $u_0$  discussed in the fol-  
 191 lowing section, we prescribe the dimensionless Dirichlet boundary condition  
 192  $w_0 = 0.1$ . Since this is an initial value problem in  $c$  and  $c_F$ , we also impose  
 193 the initial conditions,

$$c(x, z, 0) = 0, c_F(x, z, 0) = [\text{Fe}]_0, \quad (13)$$

194 where  $[\text{Fe}]_0$  is a constant. In our numerical simulations, we vary  $[\text{Fe}]_0$  to test  
 195 the effect of different mantle iron abundances on the stability of carbonated  
 196 melts.

## 197 2.2. Nondimensionalization

198 We nondimensionalize the governing equations using the following scheme,

$$\begin{aligned} \mathbf{x} &= H\mathbf{x}^*, \quad \mathbf{u} = u_0\mathbf{u}^*, \quad p = \Delta\rho_0 g H p^*, \\ \Gamma_c &= \Gamma_0 \Gamma^*, \quad \Gamma_F = \alpha \Gamma_0 \Gamma^*, \quad f_c = f_0 f_c^*, \end{aligned} \tag{14}$$

199 where the characteristic melt velocity  $u_0 = (\kappa_0 \Delta\rho_0 g) / \mu$ ,  $H$  is the height of  
 200 the LVL, and  $f_0$  is a constant arising from the rate of carbon input to the  
 201 LVL from the subducting slab. We discuss the method for calculating the  
 202 value of  $f_0$  below. Time is scaled by the dimensional constant  $t_0 = H/u_0$ .  
 203 Since the concentrations  $c$  and  $c_F$  are dimensionless, they are not scaled by  
 204 any dimensional quantities.

205 Depending on the amount of dissolved  $\text{CO}_2$  and  $\text{H}_2\text{O}$ , experimentally  
 206 determined density of silicate melts can be almost same as the density of  
 207 the mantle or as low as  $3000 \text{ kg/m}^3$  (Duncan and Agee, 2011, 0–20wt%  
 208 dissolved  $\text{CO}_2$  and 0–10wt% dissolved  $\text{H}_2\text{O}$  in silicate melt). The density  
 209 of silicate melts containing more than 20 wt% dissolved  $\text{CO}_2$  is likely even  
 210 lower. Assuming a solid density of  $3500 \text{ kg/m}^3$  (Dziewonski and Anderson,  
 211 1981) in combination with the measurements of Duncan and Agee (2011),  
 212 we estimate a range of  $\Delta\rho_0 = 10 - 500 \text{ kg/m}^3$ , which we used to constrain  
 213  $u_0$  as discussed below. The only dimensional quantity directly affected by  
 214 the choice of reference melt density is the mass flux of carbonate-rich melt  
 215 in equation (21). Due to the high concentration of dissolved  $\text{CO}_2$  in the

carbonate-rich melts, we use a conservative estimate of melt density,  $\rho = 3000 \text{ kg/m}^3$ , in evaluating fluxes. The possible uncertainty in the estimate of the flux arising from the choice of melt density however, is significantly smaller than the variations in flux arising from other parameters such as rate of carbonate supply, redox freezing rate, and time. These variations are discussed in detail in Section 4.1.

We constrain the possible range of values for  $u_0$  by considering variations in melt volume fraction and concentration of dissolved carbonate in the melt within the LVL. We use an LVL permeability range of  $10^{-15} - 10^{-14} \text{ m}^2$  (Hier-Majumder and Courtier, 2011),  $\Delta\rho_0 = 10 - 500 \text{ kg/m}^3$ ,  $\mu = 0.01 - 0.1 \text{ Pas}$  (Liebske et al., 2005), and  $g = 10 \text{ m/s}^2$ , leading to  $u_0 = 0.3 - 16 \text{ mm/yr}$ . Selecting a higher value of  $u_0$  will lead to a shorter time available for reaction between the melt and the mantle and can underestimate the influence of redox freezing on the stability of the carbonate-rich melt. To address this issue, we use a conservative value of  $u_0 = 1 \text{ mm/yr}$  as the characteristic velocity for our simulations. Combined with a characteristic length of  $H = 40 \text{ km}$ , typical height of the LVL (Hier-Majumder and Tauzin, 2017), this leads to a characteristic time  $t_0 = 40 \text{ Ma}$ .

After dropping the asterisks from the nondimensional variables, the nondimensional forms of governing equations are rewritten as

$$\phi \mathbf{u} = -\kappa (\nabla p - (1 - \gamma^* c) \hat{\mathbf{z}}), \quad (15)$$

$$\nabla \cdot \mathbf{u} = 0, \quad (16)$$

$$\frac{\partial c}{\partial t} + \mathbf{u} \cdot \nabla c = \frac{1}{\mathcal{P}e} \nabla^2 c - \mathcal{D}a \left( \frac{cc_F^2}{\phi} \right) + \beta f_c, \quad (17)$$

$$\frac{\partial c_F}{\partial t} = -\mathcal{D}a \left( \frac{\alpha cc_F^2}{1 - \phi} \right), \quad (18)$$



239 where

$$\mathcal{P}e = \frac{u_0 H}{D}, \mathcal{D}a = \frac{\Gamma_0 H}{u_0}, \beta = \frac{f_0 H}{\phi u_0}, \quad (19)$$

240 and  $\gamma^* = -1$ . The Péclet number,  $\mathcal{P}e$ , represents the ratio between rates  
241 of mass transfer by fluid percolation and chemical diffusion. The Dämmkohler  
242 number,  $\mathcal{D}a$ , is the ratio between rates of chemical reaction and fluid per-  
243 colation. The quantity  $\beta$  is a constant indicating carbonate input rate. We  
244 list the values used in this article and their suggested ranges in Table 1.  
245 Determining the value of  $\mathcal{D}a$  is difficult due to a relatively limited set of  
246 experimental data on the reaction rates under the conditions used in this  
247 study (Martirosyan et al., 2016). A recent experimental determination of  $\mathcal{D}a$   
248 and  $\mathcal{P}e$  by Pec et al. (2015) suggests  $\mathcal{D}a$  varies between 0.05 to 0.4, while  
249  $\mathcal{P}e$  varies between 0 to  $10^6$ . In contrast, the study of melt channelization by  
250 reaction infiltration instability by Spiegelman et al. (2001) suggest a range  
251 of  $\mathcal{D}a$  and  $\mathcal{P}e$  between 10 and 160. We use a larger range of  $\mathcal{D}a$  in order  
252 to provide a more conservative estimate for melt stability under more ex-  
253 treme conditions than in the experiments of Pec et al. (2015). We performed  
254 numerical simulations with the value of  $\mathcal{D}a$  ranging up to 500. In a few  
255 additional test simulations with yet higher values of  $\mathcal{D}a$ , we failed to detect  
256 any appreciable changes within geologically relevant times. While Pec et al.  
257 (2015) suggest that the value of  $\mathcal{P}e$  should be  $\mathcal{O}(10^6)$ , we confined our sim-  
258 ulations to values of  $\mathcal{P}e$  ranging between 0 and  $10^3$ . For higher values of  
259  $\mathcal{P}e$ , fluctuations in the carbon flux out of the LVL were too high to obtain a  
260 steady value for comparison with global C cycle models. We calculated the  
261 remaining dimensionless number  $\beta$  from published estimates of subducted  
262 carbon.

**Table 1:** Nondimensional numbers and dimensional constants used in this article.

Parameter	Definition	Values
$\mathcal{D}a$	Ratio between rates of chemical reaction and fluid percolation	$0 - 500^\dagger$ ( $0.05-0.4^a$ )
$\mathcal{P}e$	Ratio between rates of mass transfer by fluid percolation and diffusion	$0 - 10^{3\dagger}$ ( $10^{6,a}$ )
$\beta$	Carbon input from subduction	$0 - 5^\dagger$
$[\text{Fe}]_0$	Mantle metallic iron concentration	$0.01 - 0.1^\dagger$ ( $0.01^b$ )
$H$	Height of the domain	40 km $^\dagger, c$
$L$	Length of domain	160 km $^\dagger, c$
$S$	Surface area of the LVL	$1.8 \times 10^6$ km <sup>2</sup> $^\dagger, c$
$\Delta\rho_0$	Density difference between mantle rocks and silicate melts	500 kg/m <sup>3</sup> $^\dagger, d$
$\rho_s$	Density of mantle rocks	3500 kg/m <sup>3</sup> $^\dagger, e$
$\phi$	Melt fraction	0.01 $^\dagger, c$
$u_0$	Melt velocity	1 mm/yr $^\dagger$
$h$	Thickness of subducted carbonate layer	0.3 – 7 km $^\dagger, f$
$v_s$	Subduction rate	30 – 90 mm/yr $^\dagger, f$
$c_s$	Carbon concentration in subducted oceanic crust	0 – 7 wt% $^\dagger, f$

$^\dagger$ Values used in this article. Sources:  $^a$ Pec et al. (2015),  $^b$ Frost et al. (2004),  $^c$ Hier-Majumder and Tauzin (2017),  $^d$ (estimated from Duncan and Agee, 2011),  $^e$ Dziewonski and Anderson (1981),  $^f$ [Clift (2017); Plank (2014)]

263 The carbon input rate  $f_0$  is defined as the mass fraction of carbon sub-  
 264 ducted to the deep mantle per unit time. For a slab subducting with a ve-  
 265 locity  $v_s$ , and carbon concentration of  $c_s$ , the mass fraction of carbon added  
 266 to the LVL per unit time is given by  $f_0 = (v_s h c_s)/(HL)$ , where  $L$  is the  
 267 length of the LVL, and  $h$  is the thickness of carbonate-rich material in the  
 268 subducting slab. Substituting this  $f_0$  in the definition of  $\beta$ , we get,

$$\beta = \frac{h v_s c_s}{\phi u_0 L}. \quad (20)$$

269 The range of values of  $\beta$  used in this manuscript is listed in Table 1.

270 We calculate the  $\text{CO}_2$  flux from the LVL,  $\Phi$ , by integrating the product of  
 271 carbonate concentration in the melt, and the normal velocity over the upper  
 272 boundary of the domain  $\Omega$ ,

$$\Phi = \rho S u_0 \phi \oint_{\partial\Omega_t} c \mathbf{u} \cdot \mathbf{n} \, ds, \quad (21)$$

273 where  $\mathbf{n}$  is the outward unit normal vector on the upper boundary,  $\rho$  is the  
 274 density of the melt, and  $S$  represents the area of the LVL. The quantities  
 275 within the integral in equation (21) are dimensionless.

276 We solve the governing set of partial differential equations (15) - (18) using  
 277 a finite element formulation. Details of the finite element model are provided  
 278 in Appendix A. We carried out a number of 2D numerical simulations for  
 279 two cases. In the first case, we treated the density contrast between the melt  
 280 and solid constant. In this set of simulations, the carbonate-rich melt, when  
 281 stable, advanced through the LVL as a planar front. In a second set of simu-  
 282 lations, we considered the effect of carbonate concentration on the density of  
 283 the melt. This set of simulations generated carbonate melt-rich channelling  
 284 instabilities within the LVL. We varied four parameters,  $\mathcal{Da}$ ,  $\mathcal{Pe}$ ,  $\beta$ , and  $[\text{Fe}]_0$ ,

in our simulations. The ranges of parameter values are presented in Table 1. Finally, we studied the linearized versions of the governing equations to obtain analytical expressions for the growth rate of instabilities. We present the derivation of these linearized equations in Appendix B.

### 3. Results

In this section, we present our key results for percolation of carbonate-rich melt into the LVL. In Section 3.1, we show the numerical results for growth of planar carbonate-rich melt layers in the LVL. The results from marginal stability analysis, outlining growth rates of small perturbations in initial carbonate concentration are presented in section 3.2. Finally, we discuss the results for growth of carbonate melt-rich channelling instabilities in Section 3.3.

#### 3.1. Growth of planar fronts

When the density of carbonate-rich melt is independent of carbonate concentration, percolation of the melt from the slab to the LVL takes the shape of a planar front. We show the influence of  $\mathcal{D}a$  on the propagation and growth of this front in Figure 2(a). The colormap in this figure, and the subsequent figures, correspond to the concentration of dissolved carbonate in the melt,  $c$ . We compare six snapshots for two different values of  $\mathcal{D}a$  and three different timesteps. The values of  $\mathcal{P}e$ ,  $[\text{Fe}]_0$ , and  $\beta$  in these simulations are annotated in the figure. As the snapshots demonstrate, the growth of the planar layer is faster for the lower value of  $\mathcal{D}a$ . We notice, however, for the more realistic initial 1 wt% Fe in the mantle, the melt is not entirely consumed, even for a high value of  $\mathcal{D}a = 100$ . The planar front advances at

309 a relatively slow rate, taking nearly 240 Ma to reach the top of the 40 km  
 310 thick LVL for  $\mathcal{D}a = 1$ , and even longer for  $\mathcal{D}a = 100$ .

311 The plots in Figure 2(b) and (c) outline the dimensional flux of dissolved  
 312 carbonate atop the LVL in Mt/yr as a function of  $\mathcal{D}a$  and the carbonate  
 313 input rate,  $\beta$ , after 240 Ma. The plot of flux in panel (b) demonstrates that  
 314 for  $\beta = 1$  and  $\mathcal{D}a > 200$ , the carbonate-rich melt doesn't reach the top of the  
 315 LVL in 240 Ma, as the redox freezing consumes the carbonate in the melt.  
 316 For a value of  $\mathcal{D}a = 1$ , the flux of carbonate-rich melt atop the LVL increases  
 317 linearly with an increase in  $\beta$ . In both sets of plots in panels (b) and (c) we  
 318 compares the fluxes for two different initial Fe concentrations in the mantle.  
 319 As the results indicate, the fluxes do not show any appreciable variations  
 320 with the initial Fe content of the mantle. For the rest of this article, we only  
 321 report results for the expected natural value of  $[\text{Fe}]_0 = 0.01$  (Frost et al.,  
 322 2004). These simulations demonstrate that a planar melt layer can take 200  
 323 Ma or longer to propagate to the top of the LVL. This is the lower bound of  
 324 the growth rate, as the assumption of constant density contrast prevents the  
 325 formation of carbonate melt-rich channels discussed below.

### 326 3.2. *Marginal stability analysis*

327 In this section, we discuss the parameters influencing growth rates of small  
 328 scale instabilities. As outlined in Appendix B, we add small perturbations  
 329 of the form  $e^{ikx+\sigma t}$ , to a base state of constant carbonate concentration. The  
 330 sign of the real part of the growth rate,  $\Re(\sigma)$ , determines if the perturbations  
 331 can grow into planar or channel-like instabilities. The wavenumber of the per-  
 332 turbation,  $k$ , is the inverse of the dimensional wave length. The relationship  
 333 between the real growth rate  $\Re(\sigma)$  and the wave number  $k$  were calculated

334 by solving equation (B.9) and the real parts of the roots are plotted in Figure  
 335 3. Each plot is divided into two distinct areas (melt present or exhausted),  
 336 based on the sign of  $\Re(\sigma)$ , by the survival potential of carbonate-rich melts.

337 The marginal stability analysis predicts that melt migration should take  
 338 place by the propagation of a planar front, when the density contrast is con-  
 339 stant. As illustrated in Figure 3, the growth rate decreases with an increase  
 340 in the wavenumbers, suggesting that perturbations with smallest wavenum-  
 341 bers (largest wavelengths) will grow the fastest. This behavior implies that  
 342 melt-rich structures with large wavelengths (small wavenumbers) can sur-  
 343 vive the consumption of carbonate by chemical reactions and persist over  
 344 geologically significant periods of time. It also implies that a planar front,  
 345 characterized by an infinite wavelength will be the most dominant mode of  
 346 growth under the conditions (*i.e.* constant density contrast) considered here,  
 347 explaining the results from numerical simulations observed in section 3.1.

348 The growth rates also outline the importance of carbonate input via sub-  
 349 duction on the stability of carbonate melts in a reactive environment. The  
 350 carbonate input rate  $\beta$  tends to enhance the stability, while the reaction rate  
 351  $\mathcal{D}a$  weakens the stability of the carbonate-rich melt layer. For all cases con-  
 352 sidered in this figure, small melt channels with wavelengths less than  $\sim 1.3$   
 353 km will always be consumed by chemical reaction with the free Fe in the  
 354 mantle. The relative influences of carbon input rate ( $\beta$ ) and the chemical  
 355 reaction ( $\mathcal{D}a$ ) on the growth rate of perturbations can be observed comparing  
 356 the curves for different values of these parameters in Figure 3 (a) and (b).  
 357 As the separation between the curves indicate,  $\beta$  exerts a much stronger in-  
 358 fluence on the growth of the perturbations than  $\mathcal{D}a$ , a result we also observe

359 in the numerical simulations described next. The dominance of  $\beta$  signifies  
 360 the important role played by carbonate flux via subduction in suppressing  
 361 the effect of redox freezing.

### 362 3.3. *Melt percolation via channels*

363 This section shows the results of simulations with coupled dynamic equa-  
 364 tions (15) - (18). In all of these simulations, the density of the melt decreases  
 365 with an increase in the carbonate concentration, increasing the contrast be-  
 366 tween the melt and the solid. In contrast to the results presented in Section  
 367 3.1, we notice that the carbonate melt infiltrates into the LVL as localized  
 368 channels. Next, we outline the results of various parameters on the shape  
 369 and growth rate of these channels.

370 An increase in the  $\mathcal{P}e$  number influences the internal structure and melt  
 371 flux in two ways. First, with an increase in  $\mathcal{P}e$ , the wavelength and width of  
 372 the channels decrease. As outlined in Figure 4, simulations with weak advec-  
 373 tion ( $\mathcal{P}e = 10$ ) generates a flat interface with a relatively constant vertically  
 374 upward velocity field. In contrast, the higher  $\mathcal{P}e$  simulations (100 and 1000),  
 375 generate channels of carbonate-rich melts, with more, thinner channels for  
 376 the highest  $\mathcal{P}e$  simulation. The decrease in wavelength (increase in wave  
 377 number) of the channels with an increase in the  $\mathcal{P}e$  is consistent with the  
 378 findings from the linear stability analysis, which indicates that the wavenum-  
 379 ber varies with the square root of  $\mathcal{P}e$  (see equation (B.8) and the discussion  
 380 in Appendix B). Second, the rate of transport of carbonate-rich melt is  
 381 much faster for the higher  $\mathcal{P}e$  simulations. This faster rate of transport is  
 382 expected for a high  $\mathcal{P}e$  number, as percolative melt transfer is more dominant  
 383 under such conditions. In contrast to the planar front propagation presented

384 in Figure 2, the channels reach the top of the LVL by 80 Ma, indicating  
 385 that the reactive channelization is faster by nearly a factor of 3 in transport-  
 386 ing carbonate-rich melt into the mantle. This observation is supported by  
 387 previous models of melt propagation by reaction-infiltration-instability be-  
 388 neath midoceanic ridges (Aharonov et al., 1995; Spiegelman et al., 2001) and  
 389 carbon-sequestration by reactive flow of carbonated groundwater (Ghesmat  
 390 et al., 2011).

391 The rate of redox freezing, modulated by  $\mathcal{D}a$ , can reduce the growth rate  
 392 of melt channels. The value of  $\mathcal{D}a$  required, however, is much larger than the  
 393 natural ranges suggested by Pec et al. (2015) and Spiegelman et al. (2001).  
 394 The images in Figure 5 demonstrate this influence. While the melt channels  
 395 propagate to the top of the LVL by 80 Ma for  $\mathcal{D}a = 1$ , they only reach  
 396 halfway through the top of the LVL in the same time when  $\mathcal{D}a = 500$ . These  
 397 plots demonstrate that natural nonequilibrium processes like melt migration,  
 398 lead to the formation of features that are not permitted under equilibrium  
 399 conditions attained in the laboratory experiments.

400 The strongest influence on the formation of carbonate-rich melt zones in  
 401 the LVL is exerted by the amount of carbon input from subduction, parame-  
 402 terized by  $\beta$ . The snapshots in Figure 6 outline the influence exerted by the  
 403 magnitude of carbon transfer to the LVL by changes in this parameter. This  
 404 influence is twofold. First, as the colormaps indicate, the channels for  $\beta = 3$   
 405 are richer in dissolved carbonate and the melt propagates with a faster veloc-  
 406 ity as compared to  $\beta = 1$ . Second, by 120 Ma, fewer, but larger, channels are  
 407 established for  $\beta = 3$  compared to  $\beta = 1$ . This behavior of melt transport  
 408 due to a higher input from subduction contrasts the behavior of  $\mathcal{P}e$  number



409 as shown in Figure 4, where a larger  $Pe$  number leads to the formation of  
410 more high speed jets of melt.

## 411 4. Discussion

### 412 4.1. LVLs as potential deep carbon reservoirs

413 Our results indicate that the slab-derived carbonate melt can survive re-  
414 dox freezing for a number of subduction scenarios. We can further analyze  
415 the output from these simulations to provide an estimate, at least region-  
416 ally, for the amount of  $CO_2$  supplied to the mantle by melting of subducted  
417 carbonated oceanic crust. We calculated the dimensional fluxes of carbonate  
418 dissolved in the melt for the LVL in the western US. These fluxes outline the  
419 role played by regional LVLs in the global carbon cycle. For comparison, the  
420 global estimates of subducted  $CO_2$  varies between 88–176 Mt/yr (Dasgupta  
421 and Hirschmann, 2010) to as high as  $300 \pm 50$  Mt/yr (Plank and Manning,  
422 2019).

423 The plot in Figure 7(a) show the flux of carbonate dissolved in melt  
424 through the top of the LVL as a function of time. We compare the range of  
425 fluxes for 3 different values of  $\beta$  and 2 different values of  $\mathcal{D}a$ . The plot demon-  
426 strates that the flux is highly transient with aperiodic waxing and waning.  
427 The time interval between peak fluxes are reduced by a high carbonate sup-  
428 ply from the slab, indicated by higher values of  $\beta$ . We also notice that for  
429 a given value of  $\beta$ , peak fluxes occur earlier for lower values of  $\mathcal{D}a$ . Despite  
430 these strong variations with time, we can observe some general patterns of  
431 the flux into the mantle as a function of  $\beta$  and  $\mathcal{D}a$ .

432 Our results suggest that plate tectonics plays a crucial role in the survival

433 of carbonate melts in the LVL. The plots in Figure 7(b) and (c) show the value  
 434 of fluxes averaged over 74 to 96 Ma from the beginning of the simulation.  
 435 The vertical error bars indicate the range of variation in the flux, while the  
 436 data points represent the temporal average over this time period. While the  
 437 magnitude of the flux decreases nonlinearly with the  $\mathcal{D}a$ , it is also strongly  
 438 modified by the value of  $\beta$ , as shown by the different sets of curves. For  $\beta = 3$ ,  
 439 the output to the mantle varies between 8–25 Mt/yr, a significant fraction of  
 440 the global budget. Comparison between the curves corresponding to the two  
 441 different values of  $\mathcal{D}a$  in Figure 7(c) illustrates that a small change in  $\beta$  at a  
 442 constant  $\mathcal{D}a$  exerts a greater influence on the flux compared to changing the  
 443  $\mathcal{D}a$  by two orders of magnitude. Thus, the carbonate supply to the mantle  
 444 by subduction is the stronger control on the stability of carbonate melts in  
 445 the LVL than redox freezing. Our estimate of the carbonate flux into the  
 446 LVL assumes an area equal to the LVL observed under the western US. If the  
 447 LVL is global, however, it can act as a substantial impediment to carbonate  
 448 transport to the lower mantle.

#### 449 *4.2. Melt channels, superdeep diamonds, and ancient carbonate subduction*

450 Evidence from superdeep diamonds and their mineral inclusions indicate  
 451 an important role of slab-derived carbonated melt in their origin. A number  
 452 of features, such as crystalline morphology of the diamonds, compositions  
 453 of their mineral inclusions, and the  $\delta^{13}C$  signature of the diamonds indicate  
 454 that they are formed by reactions between carbonate-rich melts and mantle  
 455 peridotites (Bulanova et al., 2010; Smith et al., 2016; Walter et al., 2008).  
 456 Some of these diamonds grow to several centimeters in size, suggesting the ex-  
 457 istence of an environment suitable for nucleation and growth over a relatively

458 long period of time. Such an environment, conducive of diamond growth by  
459 reaction between the mantle peridotite, carbonate melt, and iron can form  
460 around the edges of carbonate-melt channels observed in our simulations.

461 Figure 8 shows the maps of concentration of Fe and carbonate in the melt  
462 following the establishment of stable channels. As the map of Fe concentra-  
463 tion indicates, partially reacted mantle domains exist around the edges of the  
464 channels. These regions can be up to several kilometers wide. As observed in  
465 the flux plots in Figures 7, these channels are established during the first 50  
466 Ma of the simulation. Following the establishment of the channels, a tran-  
467 sient supply of carbonate-rich melts over geologically significant periods of  
468 time can ensure transient periods of growth of diamonds.

## 469 5. Conclusions

470 Our results indicate that carbonate-rich melt from the subducting slab  
471 can migrate into the LVL either as a planar front or as channels. The former  
472 results are obtained when the density of the melt is independent of carbonate  
473 concentration in the melt. We also find that the rate of melt infiltration into  
474 the LVL is much slower as a planar front. Our results demonstrate that the  
475 rate of carbonate input from subduction plays a stronger role in determining  
476 the stability of carbonate melts in the LVL than the redox freezing due to  
477 the low oxygen fugacity of the mantle. We show that with carbon transport  
478 into the mantle by reactive channels, it is possible to sequester up to 25 Mt  
479 CO<sub>2</sub> per year into an LVL similar in size to the one beneath the Western  
480 US. Zones of reaction between channels and mantle can serve of domains for  
481 generation of large super-deep diamonds.

## 482 Acknowledgment

483 We acknowledge the financial supports from the National Natural Sci-  
484 ence Foundation of China (41688103), the Chinese Academy of Sciences  
485 (XDB18000000) and the State Oceanography Bureau (GASI-GEOGE-02).  
486 SH-M acknowledges support from an US NSF grant EAR 1215800. YZS  
487 is supported by a joint PhD program between the Guangzhou Institute of  
488 Geochemistry, Chinese Academy of Sciences, and Royal Holloway University  
489 of London. We appreciate suggestions from Terry Plank, Maxim Ballmer  
490 and Giulio Solferino during the preparation of the manuscript. Insightful  
491 suggestions from two anonymous reviewers and editor John Brodholt greatly  
492 helped improve the manuscript.

## 493 Appendix A. Weak Formulation

494 To solve the governing partial differential equations, we discretize the  
495 equations using a Petrov-Galerkin finite element scheme. Integrating the  
496 Darcy and continuity equations in Eqs.(15) - (16) by parts, and defining  
497 arbitrary test functions  $\mathbf{v}$  and  $q$ , we obtain the weak form

$$\int_{\Omega} (\phi \mathbf{u} \cdot \mathbf{v} - \kappa p \nabla \cdot \mathbf{v} + \nabla \cdot \mathbf{u} q) \, d\Omega = \int_{\Omega} \kappa (1 - \gamma^* c) \hat{\mathbf{z}} \cdot \mathbf{v} \, d\Omega. \quad (\text{A.1})$$

498 To solve the component mass conservation equations, we discretize the  
499 time derivative  $\partial c / \partial t$  using a Crank-Nicholson scheme, such that midway  
500 concentration  $\bar{c}$  between the previous step ( $c_0$ ) and the current step ( $c_1$ )  
501 is given by  $\bar{c} = (c_1 + c_0) / 2$ . Inserting this time derivative and integrating

equations (17) - (18) by parts, we obtain the weak formulation

$$\begin{aligned} \int_{\Omega} \left[ (c_1 - c_0) \eta + \mathbf{u} \cdot \nabla \bar{c} \Delta t \eta + \frac{\Delta t}{\mathcal{P}_e} \nabla \bar{c} \cdot \nabla \eta + (c_{F1} - c_{F0}) \omega \right] d\Omega \\ = - \int_{\Omega} \left( \frac{\mathcal{D}acc_F^2}{\phi} \Delta t \eta - \beta f_c \Delta t \eta + \frac{\alpha \mathcal{D}acc_F^2}{1 - \phi} \Delta t \omega \right) d\Omega, \end{aligned} \quad (\text{A.2})$$

where  $\eta$  and  $\omega$  are arbitrary test functions. We also notice that the Neumann boundary condition on  $c$  is naturally incorporated in this formulation.

Additionally, to reduce the oscillation, we apply standard streamline upwind Petrov-Galerkin stabilization by adding a term  $r_{\text{SUPG}}$  (Sendur, 2018)

$$r_{\text{SUPG}} = \int_{\Omega} \frac{1}{4/(\mathcal{P}_e \delta^2) + 2|\mathbf{u}|/\delta} (\mathbf{u} \cdot \nabla \eta) r d\Omega, \quad (\text{A.3})$$

where  $\delta$  is the cell diameter,  $|\mathbf{u}|$  is the norm of the melt velocity, and the residual  $r$  is given by

$$\begin{aligned} r = (c_1 - c_0) + \left( \mathbf{u} \cdot \nabla \bar{c} - \frac{\nabla^2 c}{\mathcal{P}_e} + \frac{\mathcal{D}acc_F^2}{\phi} - \beta f_c \right) \Delta t \\ + (c_{F1} - c_{F0}) + \frac{\alpha \mathcal{D}acc_F^2}{1 - \phi} \Delta t. \end{aligned} \quad (\text{A.4})$$

## Appendix B. Linearized Equations

The first order influence of the key dimensionless parameters on the growth rate and internal structure of the LVL can be determined by marginal stability analysis. In this analysis, we consider a base state defined by the absence of carbonate influx from slabs and porous flow. The base state is also characterized by constant concentrations of carbonate in the melt ( $c_0$ ) and Fe in the mantle ( $c_{F0}$ ). We then perturb this base state by adding small fluctuations in the concentrations of carbonate input from the slab and a first order chemical reaction between the melt and the mantle (Ghesmat et al.,

2011), and study the growth of these perturbations. The values of concentrations and the source term can then be written as a sum of the base state and the perturbed state,

$$c = c_0 + \epsilon \bar{c}(z) e^{ikx + \sigma t}, \quad (\text{B.1})$$

$$c_F = c_{F0} + \epsilon \bar{c}_F(z) e^{ikx + \sigma t}, \quad (\text{B.2})$$

$$f_c = \epsilon \bar{f}_c(z) e^{ikx + \sigma t}, \quad (\text{B.3})$$

where  $\epsilon \ll 1$  is a constant,  $k$  is the nondimensional wave number, and  $\sigma$  is the growth rate of perturbations, respectively. While the wavenumber  $k$  is purely real,  $\sigma$  is complex, its real part,  $\Re(\sigma)$ , contributes to the growth of the perturbations while the imaginary part,  $\Im(\sigma)$ , is the frequency of the wave-like solution to the governing equations.

Based on the definition above, we substitute equations (B.1) to (B.3) into equations (15) to (18) and set  $\bar{f}_c = \bar{c}$ . The resulting linearized equation on  $\mathcal{O}(\epsilon)$  can be simplified to the ODE for an undamped harmonic oscillator (Ghesmat et al., 2011),

$$\frac{d^2 \bar{c}}{dz^2} = \omega^2 \bar{c}, \quad (\text{B.4})$$

where

$$\omega^2 = k^2 + \mathcal{P}e \left( \sigma + \frac{\mathcal{D}a}{\phi} \frac{(1 - \phi) \sigma c_{F0}}{(1 - \phi) \sigma + \mathcal{D}a c_0} - \beta \right). \quad (\text{B.5})$$

We seek a solution to equation (B.4) for a zero-flux Neumann boundary condition and a zero concentration Dirichlet boundary condition at the slab interface, given by,

$$\left. \frac{d\bar{c}}{dz} \right|_{z=0} = 0, \quad \text{and} \quad \bar{c}|_{z=0} = 0. \quad (\text{B.6})$$

534 One specific solution for the ODE in equation (B.4), subject to these bound-  
 535 ary conditions can take the form

$$\bar{c} = A_1 (1 - e^{\omega z}), \quad (\text{B.7})$$

536 where  $A_1$  is a constant (Ghesmat et al., 2011). It can be shown that the only  
 537 nontrivial specific solution of the form in equation (B.7) which satisfies both  
 538 boundary conditions, exists when  $\omega = 0$ . Using this condition, we can derive  
 539 a relation between the growth rate as a function of the dimensionless wave  
 540 number,  $k$ , for two cases.

541 In the first case, we assume that the mantle is iron-free in the base state,  
 542 leading to  $c_{F0} = 0$ . This case is also true if  $\mathcal{D}a = 0$ . Under this condition,  
 543 for  $\omega = 0$ , equation (B.5) leads to the relation between  $\sigma$  and  $k$ ,

$$\sigma = \beta - \frac{k^2}{\mathcal{P}e}. \quad (\text{B.8})$$

544 Since both  $\beta$  and  $\mathcal{P}e$  are real, the growth rate is real in this case. The  
 545 perturbations in concentration either grow or decay, depending on the sign  
 546 of  $\sigma$ . We also notice that to sustain growth ( $\sigma > 0$ ) for a constant  $\beta$ , the  
 547 wavenumber should scale with  $\sqrt{\mathcal{P}e}$ . As a result, high values of  $\mathcal{P}e$  will force  
 548 growth of perturbations with higher values of  $k$ , resulting in the growth of  
 549 many small wavelength channels, as observed in the numerical simulations.

550 In the second case,  $c_{F0}, \mathcal{D}a \neq 0$ . For this condition, equation (B.5) can  
 551 be rewritten as a quadratic equation in  $\sigma$ ,

$$A\sigma^2 + B\sigma + C = 0, \quad (\text{B.9})$$

552 where

$$\begin{aligned} A &= \mathcal{P}e\phi(1 - \phi), \\ B &= \mathcal{D}a[\mathcal{P}e\phi c_0 + (1 - \phi)c_{F0}] + \phi(1 - \phi)(k^2 - \mathcal{P}e\beta), \\ C &= \mathcal{D}ac_0\phi(k^2 - \mathcal{P}e\beta). \end{aligned} \tag{B.10}$$

553 The quadratic equation in  $\sigma$  yields two complex roots. As discussed above,  
554 only  $\Re(\sigma)$  contributes to the decay or growth of the perturbations. We  
555 extract  $\Re(\sigma)$  from the solution and discuss the implications in Section 3.2.

## 556 References

- 557 Agius, M. R., Rychert, C. A., Harmon, N., Laske, G., 2017. Mapping the  
558 mantle transition zone beneath Hawaii from Ps receiver functions : Evi-  
559 dence for a hot plume and cold mantle downwellings. *Earth and Planetary*  
560 *Science Letters* 474, 226–236.
- 561 Aharonov, E., Whitehead, J. A., Kelemen, P. B., Spiegelman, M., 1995.  
562 Channelling instability of upwelling melt in the mantle. *Journal of Geo-*  
563 *physical Research: Solid Earth* 100 (B10), 20433–20450.
- 564 Bercovici, D., Ricard, Y., Schubert, G., 2001. A two-phase model for com-  
565 paction and damage: 1. General Theory. *Journal of Geophysical Research:*  
566 *Solid Earth* 106 (B5), 8887–8906.
- 567 Bulanova, G. P., Walter, M. J., Smith, C. B., Kohn, S. C., Armstrong, L. S.,  
568 Blundy, J., Gobbo, L., 2010. Mineral inclusions in sublithospheric dia-  
569 monds from Collier 4 kimberlite pipe, Juina, Brazil: Subducted protoliths,  
570 carbonated melts and primary kimberlite magmatism. *Contributions to*  
571 *Mineralogy and Petrology* 160 (4), 489–510.



572 Burnham, A. D., Thomson, A. R., Bulanova, G. P., Kohn, S. C., Smith,  
573 C. B., Walter, M. J., dec 2015. Stable isotope evidence for crustal recycling  
574 as recorded by superdeep diamonds. *Earth and Planetary Science Letters*  
575 432, 374–380.

576 Christensen, U., 2001. Geodynamic models of deep subduction. *Physics of*  
577 *the Earth and Planetary Interiors* 127 (1-4), 25–34.

578 Christensen, U. R., 1996. The influence of trench migration on slab penetra-  
579 tion into the lower mantle. *Earth and Planetary Science Letters* 140 (1–4),  
580 27–39.

581 Christensen, U. R., Yuen, D. A., 1984. The interaction of a subducting litho-  
582 spheric slab with a chemical or phase boundary. *Journal of Geophysical*  
583 *Research: Solid Earth* 89 (B6), 4389–4402.

584 Čížková, H., van Hunen, J., van den Berg, A. P., Vlaar, N. J., 2002. The  
585 influence of rheological weakening and yield stress on the interaction of  
586 slabs with the 670 km discontinuity. *Earth and Planetary Science Letters*  
587 199 (3-4), 447–457.

588 Clift, P. D., 2017. A revised budget for Cenozoic sedimentary carbon sub-  
589 duction. *Reviews of Geophysics* 55 (1), 97–125.

590 Dasgupta, R., Hirschmann, M. M., 2010. The deep carbon cycle and melting  
591 in Earth’s interior. *Earth and Planetary Science Letters* 298 (1-2), 1–13.

592 Dorfman, S. M., Badro, J., Nabiei, F., Prakapenka, V. B., Cantoni, M.,  
593 Gillet, P., 2018. Carbonate stability in the reduced lower mantle. *Earth*  
594 *and Planetary Science Letters* 489, 84–91.

595 Duncan, M. S., Agee, C. B., 2011. The partial molar volume of carbon dioxide  
596 in peridotite partial melt at high pressure. *Earth and Planetary Science*  
597 *Letters* 312 (3-4), 429–436.

598 Dziewonski, A. M., Anderson, D. L., jun 1981. Preliminary reference Earth  
599 model. *Physics of the Earth and Planetary Interiors* 25 (4), 297–356.

600 Frost, D. J., Liebske, C., Langenhorst, F., McCammon, C. A., Trønnes, R. G.,  
601 Rubie, D. C., 2004. Experimental evidence for the existence of iron-rich  
602 metal in the Earth’s lower mantle. *Nature* 428 (6981), 409.

603 Ghesmat, K., Hassanzadeh, H., Abedi, J., 2011. The impact of geochemistry  
604 on convective mixing in a gravitationally unstable diffusive boundary layer  
605 in porous media: CO<sub>2</sub> storage in saline aquifers. *Journal of Fluid Mechanics*  
606 673, 480–512.

607 Griffiths, R. W., Hackney, R. I., van der Hilst, R. D., 1995. A laboratory  
608 investigation of effects of trench migration of the descent of subducted  
609 slabs. *Earth and Planetary Science Letters* 133, 1–17.

610 Harte, B., 2010. Diamond formation in the deep mantle: the record of mineral  
611 inclusions and their distribution in relation to mantle dehydration zones.  
612 *Mineralogical Magazine* 74, 189–215.

613 Hier-Majumder, S., 2018. Analytical solution for two-phase flow within and  
614 outside a sphere under pure shear. *Journal of Fluid Mechanics* 848, 987–  
615 1012.

616 Hier-Majumder, S., Courtier, A., 2011. Seismic signature of small melt frac-  
617 tion atop the transition zone. *Earth and Planetary Science Letters* 308 (3-  
618 4), 334–342.

619 Hier-Majumder, S., Hirschmann, M. M., 2017. The origin of volatiles in the  
620 Earth’s mantle. *Geochemistry Geophysics Geosystems* 18 (1), 1–12.

621 Hier-Majumder, S., Keel, E., Courtier, A., 2014. The influence of tempera-  
622 ture, bulk composition, and melting on the seismic signature of the low  
623 velocity layer above the transition zone. *Journal of Geophysical Research:*  
624 *Solid Earth* 119 (2), 971–983.

625 Hier-Majumder, S., Ricard, Y., Bercovici, D., 2006. Role of grain boundaries  
626 in magma migration and storage. *Earth and Planetary Science Letters*  
627 248 (3-4), 735–749.

628 Hier-Majumder, S., Tauzin, B., 2017. Pervasive upper mantle melting be-  
629 neath the western US. *Earth and Planetary Science Letters* 463, 25–35.

630 Hirschmann, M. M., Dasgupta, R., 2009. The H/C ratios of Earth’s near-  
631 surface and deep reservoirs, and consequences for deep Earth volatile cy-  
632 cles. *Chemical Geology* 262 (1-2), 4–16.

633 Ickert, R. B., Stachel, T., Stern, R. A., Harris, J. W., 2015. Extreme  $^{18}\text{O}$ -  
634 enrichment in majorite constrains a crustal origin of transition zone dia-  
635 monds. *Geochemical Perspectives Letters* 1 (1), 65–74.

636 Li, S. G., Yang, W., Ke S, Meng, X. N., Tian, H. C., Xu, L. J., He, Y. S.,  
637 Huang, J., Wang, X. C., Xia, Q. K., Sun, W. D., Yang, X. Y., Ren, Z. Y.,

638 Wei, H. Q., Liu, Y. S., Meng, F. C., J., Y., 2017. Deep carbon cycles  
 639 constrained by a large-scale mantle Mg isotope anomaly in eastern China.  
 640 National Science Review 4, 111–120.

641 Liebske, C., Schmickler, B., Terasaki, H., Poe, B., Suzuki, a., Funakoshi, K.,  
 642 Ando, R., Rubie, D., 2005. Viscosity of peridotite liquid up to 13 GPa:  
 643 Implications for magma ocean viscosities. Earth and Planetary Science  
 644 Letters 240 (3-4), 589–604.

645 Martirosyan, N. S., Yoshino, T., Shatskiy, A., Chanyshiev, A. D., Litasov,  
 646 K. D., 2016. The  $\text{CaCO}_3$ –Fe interaction: Kinetic approach for carbonate  
 647 subduction to the deep Earths mantle. Physics of the Earth and Planetary  
 648 Interiors 259, 1–9.

649 Ohtani, E., Litasov, K., Hosoya, T., Kubo, T., Kondo, T., 2004. Water  
 650 transport into the deep mantle and formation of a hydrous transition zone.  
 651 Physics of the Earth and Planetary Interiors 143, 255–269.

652 Pec, M., Holtzman, B. K., Zimmerman, M., Kohlstedt, D. L., 2015. Reaction  
 653 infiltration instabilities in experiments on partially molten mantle rocks.  
 654 Geology 43 (7), 575–578.

655 Plank, T., 2014. The chemical composition of subducting sediments. Treatise  
 656 on geochemistry 4, 607–629.

657 Plank, T., Manning, C. E., 2019. Subducting carbon. Nature 574 (7778),  
 658 343–352.

659 Rhebergen, S., Wells, G. N., Katz, R. F., Wathen, A. J., 2014. Analysis

660 of block preconditioners for models of coupled magma/mantle dynamics.  
661 SIAM Journal on Scientific Computing 36 (4), A1960–A1977.

662 Rohrbach, A., Schmidt, M. W., 2011. Redox freezing and melting in the  
663 Earths deep mantle resulting from carbon–iron redox coupling. Nature  
664 472 (7342), 209.

665 Sendur, A., 2018. A comparative study on stabilized finite element methods  
666 for the convection-diffusion-reaction problems. Journal of Applied Mathe-  
667 matics 2018, 1–16.

668 Smith, E. M., Shirey, S. B., Nestola, F., Bullock, E. S., Wang, J., Richardson,  
669 S. H., Wang, W., 2016. Large gem diamonds from metallic liquid in Earths  
670 deep mantle. Science 354 (6318), 1403–1405.

671 Spiegelman, M., Kelemen, P. B., Aharonov, E., 2001. Causes and conse-  
672 quences of flow organization during melt transport: The reaction infil-  
673 tration instability in compactible media. Journal of Geophysical Research  
674 106 (B2), 2061–2077.

675 Steefel, C. I., Lasaga, A. C., 1994. A coupled model for transport of multiple  
676 chemical species and kinetic precipitation/dissolution reactions with ap-  
677 plication to reactive flow in single phase hydrothermal systems. American  
678 Journal of Science 294 (5), 529–592.

679 Takei, Y., Hier-Majumder, S., oct 2009. A generalized formulation of inter-  
680 facial tension driven fluid migration with dissolution/precipitation. Earth  
681 and Planetary Science Letters 288 (1-2), 138–148.

682 Tauzin, B., Debayle, E., Wittlinger, G., 2010. Seismic evidence for a global  
683 low-velocity layer within the Earths upper mantle. *Nature Geoscience*  
684 3 (10), 718.

685 Tauzin, B., Kim, S., Kennett, B. L. N., 2017. Pervasive seismic low-velocity  
686 zones within stagnant plates in the mantle transition zone: Thermal or  
687 compositional origin? *Earth and Planetary Science Letters* 477, 1–13.

688 Tauzin, B., van der Hilst, R. D., Wittlinger, G., Ricard, Y., 2013. Multiple  
689 transition zone seismic discontinuities and low velocity layers below west-  
690 ern United States. *Journal of Geophysical Research: Solid Earth* 118 (5),  
691 2307–2322.

692 Thomson, A. R., Kohn, S. C., Bulanova, G. P., Smith, C. B., Araujo, D. P.,  
693 EIMF, Walter, M. J., 2014. Origin of sublithospheric diamonds from the  
694 Juina-5 kimberlite (Brazil): Constraints from carbon isotopes and inclu-  
695 sion compositions. *Contributions to Mineralogy and Petrology* 168 (6),  
696 1081.

697 Thomson, A. R., Walter, M. J., Kohn, S. C., Brooker, R. A., 2016. Slab  
698 melting as a barrier to deep carbon subduction. *Nature* 529 (7584), 76.

699 Turcotte, D., Schubert, G., 2001. *Geodynamics*. John Willey & Sons.

700 Unwin, H. J. T., Wells, G. N., Woods, A. W., 2016. CO<sub>2</sub> dissolution in a  
701 background hydrological flow. *Journal of Fluid Mechanics* 789, 768–784.

702 Walter, M. J., Bulanova, G. P., Armstrong, L. S., Keshav, S., Blundy, J. D.,  
703 Gudfinnsson, G., Lord, O. T., Lennie, A. R., Clark, S. M., Smith, C. B.,

- 704 Gobbo, L., 2008. Primary carbonatite melt from deeply subducted oceanic  
705 crust. *Nature* 454 (7204), 622.
- 706 Wei, S. S., Shearer, P. M., 2017. A sporadic low-velocity layer atop the 410 km  
707 discontinuity beneath the Pacific Ocean. *Journal of Geophysical Research:*  
708 *Solid Earth* 122 (7), 5144–5159.
- 709 Xu, Y. G., Li, H. Y., Hong, L. B., 2018. Generation of Cenozoic intraplate  
710 basalts in the big mantle wedge under eastern Asia. *Science China Earth*  
711 *Sciences* 61 (7), 869–886.

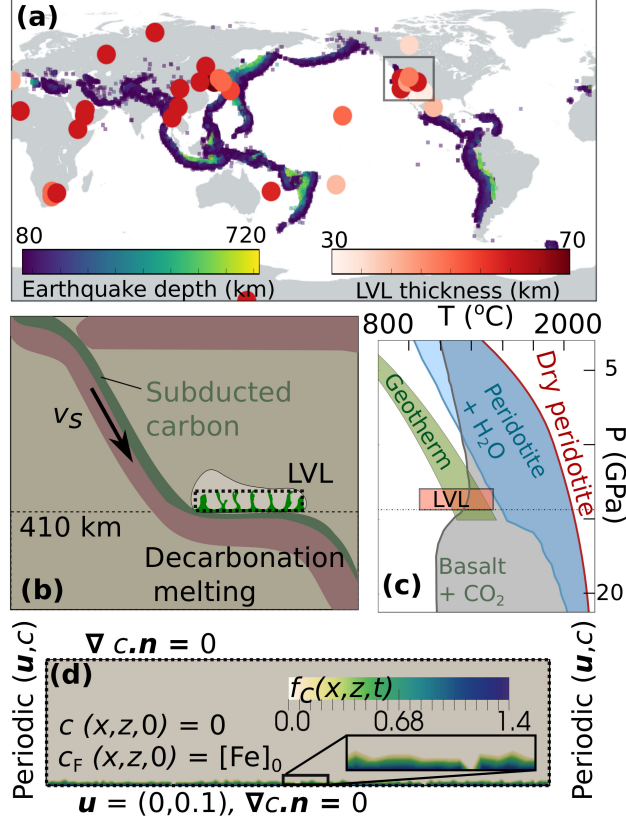


**Figure 1:** (a) Global distribution of 350 - 410 km low-velocity layers above the transition zone (references in Wei and Shearer, 2017). The colormap indicates that the median of LVL thicknesses is around 40 - 60 km. (b) A schematic diagram outlining the site of decarbonation melting atop a stalled slab. The rectangle with broken outline is the domain of our problem, magnified in panel (d). (c) The phase diagram of solidi of dry peridotite (Hier-Majumder and Hirschmann, 2017), wet peridotite (Ohtani et al., 2004), and carbonated basalt (Thomson et al., 2016). The light green area marks the range of slab geotherms for slab velocities ranging from 7 to 10 cm/yr. The horizontal shaded box indicates the P-T range of the LVL beneath the western US (Hier-Majumder and Tausin, 2017), shown as the open, black rectangle in panel (a). (d) A schematic diagram of the domain used in our numerical simulations. The boundary and initial conditions are annotated in the figure. Also shown is a colormap of the dimensionless source term  $f_c$ . The box in the inset is a magnification of the region enclosed by the rectangle at the bottom.



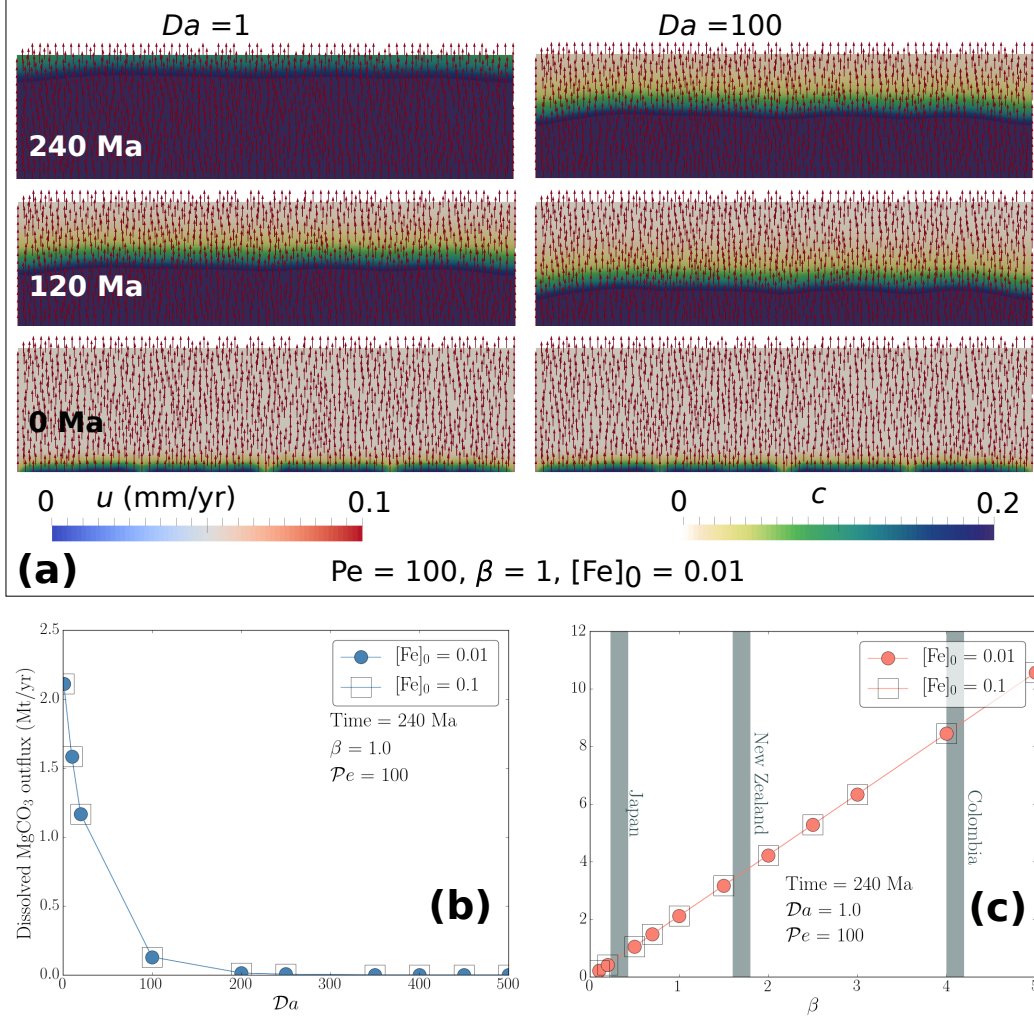


**Figure 2:** (a) Results from numerical simulations with  $\beta = 1$ ,  $Pe = 100$ , and  $[Fe]_0 = 0.01$ . The colormap shows wt% of carbonates in the melt for two different values of  $Da$  for three different dimensional times. Dimensional flux of dissolved carbonate, calculated from equation (21), atop the LVL after 240 Ma as a function of (b)  $Da$  and (c)  $\beta$  for two different initial values of Fe concentration in the mantle. The estimates for  $\beta$  for the different subduction settings were calculated from the GLOSS II model of Plank (2014) and the dimensional constants used in the calculation are listed in Table 1.

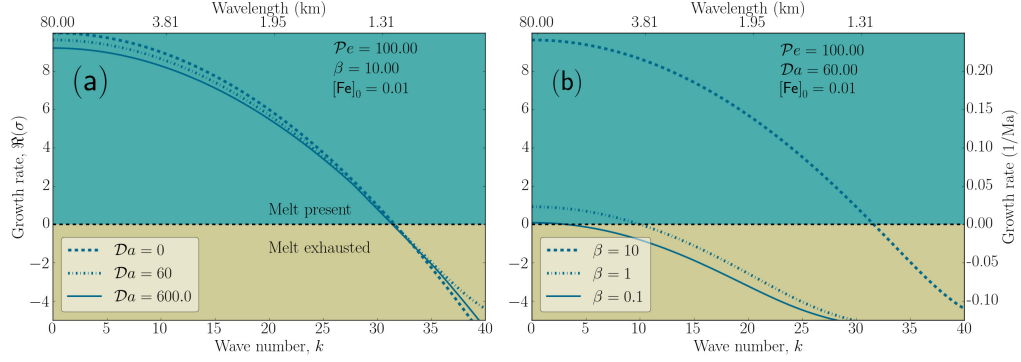


**Figure 3:** Results from marginal stability analysis. (a) Plots of the real part of the dimensionless growth rate  $\Re(\sigma)$  as a function of dimensionless wave number  $k$  for different values of  $Da$ . (b) Plots of the growth rate for different values of  $\beta$ . A partially molten layer will be exhausted by chemical reactions for  $\Re(\sigma) < 0$ .

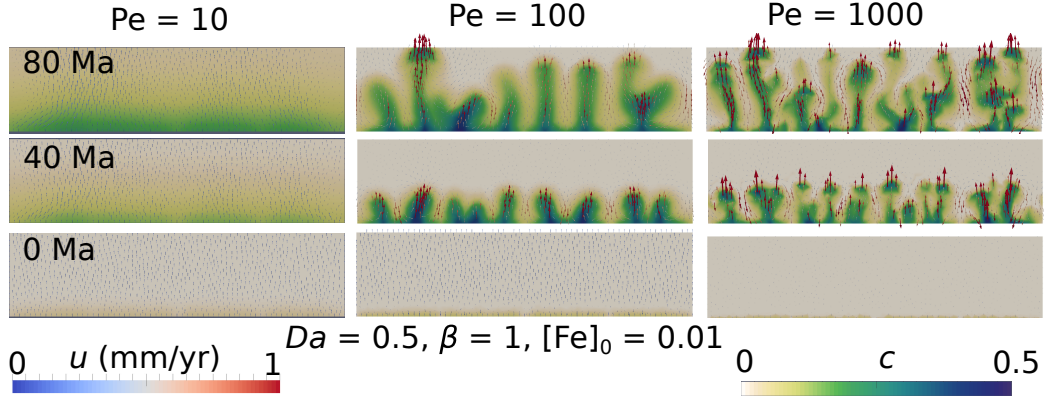


**Figure 4:** The effect of  $Pe$  on melt transport for simulations with  $Da = 0.5$ ,  $\beta = 1.0$ , and  $[Fe]_0 = 0.01$ . The colormaps show wt% of carbonates in the melt and the magnitude of the melt velocity, respectively.

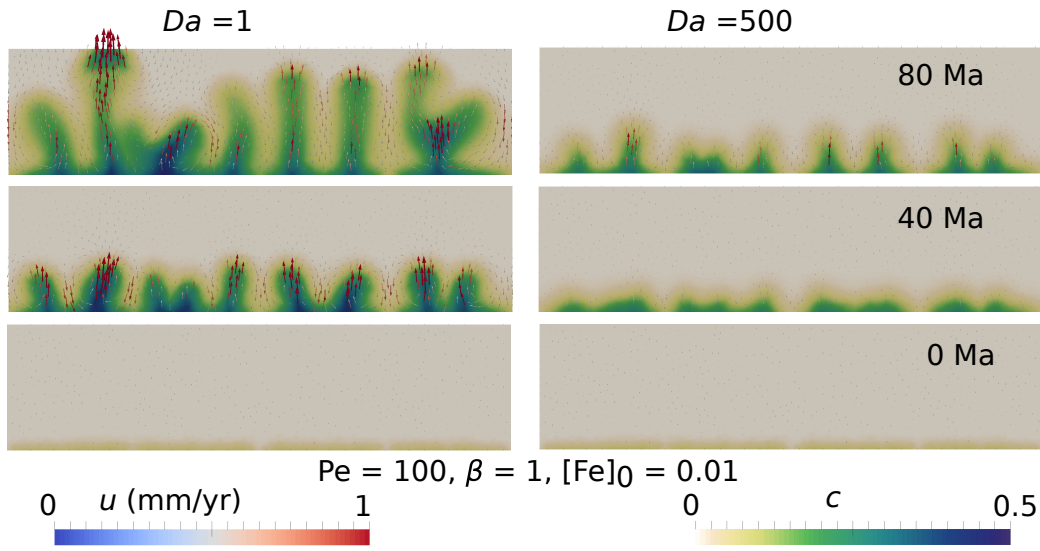


**Figure 5:** The effect of reaction rates  $Da$  for simulations with  $Pe = 100$ ,  $\beta = 1.0$ , and  $[Fe] = 0.01$ . The colormaps show wt% of carbonates in the melt and the magnitude of the melt velocity, respectively.

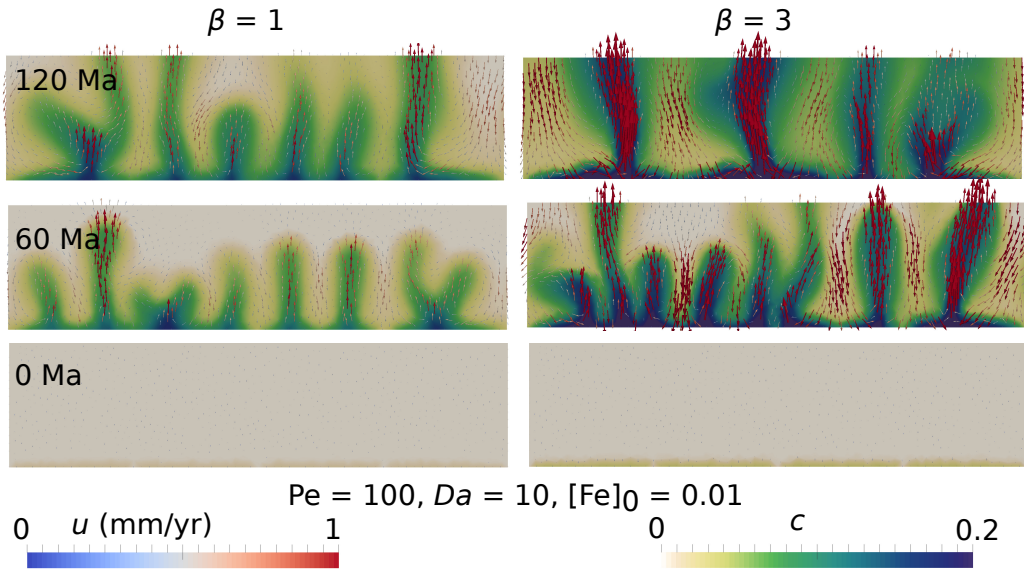


**Figure 6:** The effect of  $\beta$  for simulations with  $Da = 10$ ,  $Pe = 100$ , and  $[Fe] = 0.01$ . The colormaps show wt% of carbonates in the melt and the magnitude of the melt velocity, respectively.

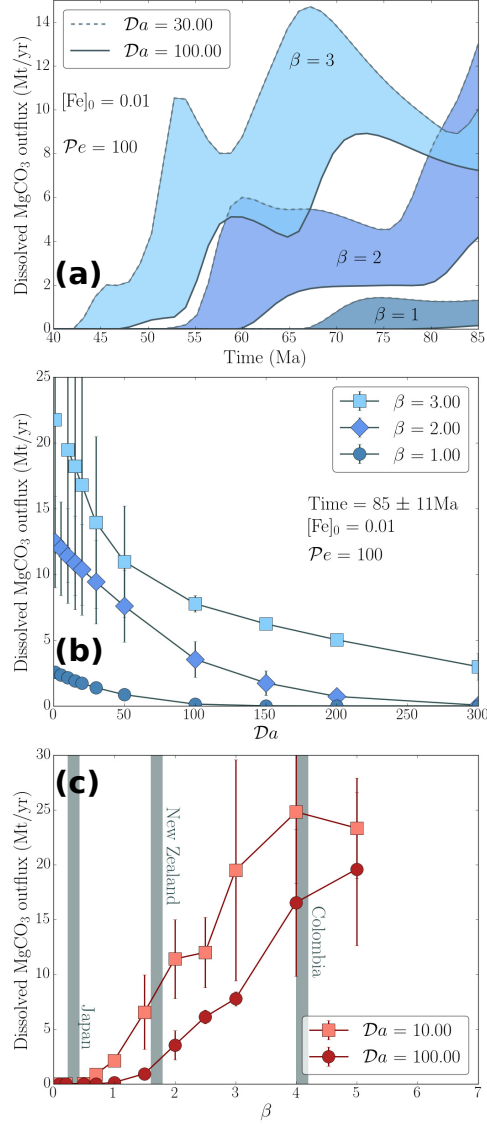


**Figure 7:** (a) Dimensional outflux of dissolved carbonate as a function of time for 3 different values of  $\beta$ . For each value of  $\beta$ , two different  $Da$  values are used. Plot of outflux of dissolved carbonate averaged over 74 to 96 Ma, as a function of (b)  $Da$  and (c)  $\beta$ . The vertical error bars represent the standard deviation of the flux over this time period.

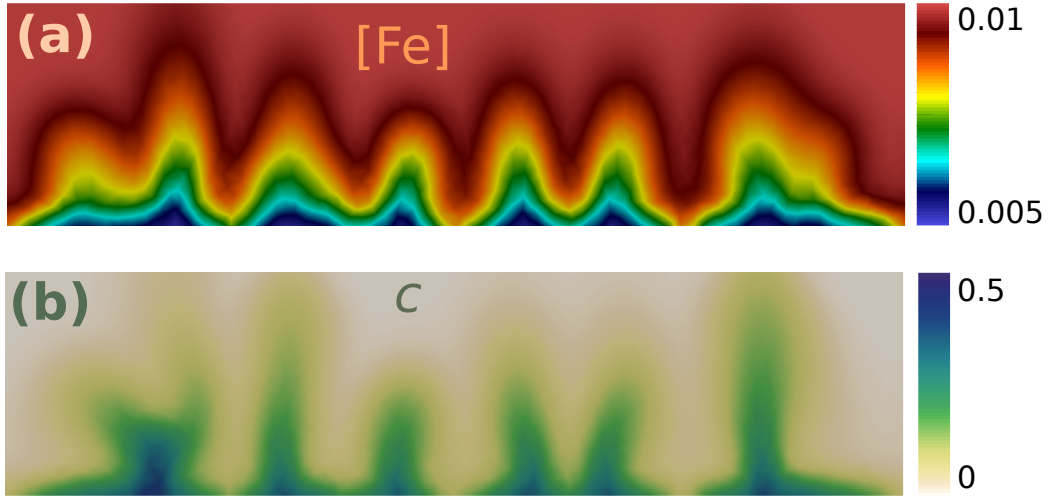


**Figure 8:** Concentration maps of solid Fe in the mantle (top) and dissolved CO<sub>2</sub> in the melt (bottom), from a simulation with  $Da = 100$ ,  $Pe = 100$ , and  $\beta = 1$  after 120 Ma. The initial Fe concentration in the mantle was 0.01.